



Microstructural evolution and mechanical properties of FeCrNiCuTi_x high entropy alloys

Sheng Fang ^{a,b,d}, Long Meng ^{b,c,d,*}, Yang Li ^{b,d}, Kejia Liu ^{b,d}, Lingsheng Ke ^{b,d}, Wanying Fu ^c, Tao Qi ^{a,b,c,d,**}

^a School of Physics and Materials, Nanchang University, Nanchang, 330000, China

^b Ganjiang Innovation Academy, Chinese Academy of Sciences, Ganzhou, 341000, China

^c Institute of Process Engineering, Chinese Academy of Sciences, Beijing, 100190, China

^d Jiangxi Province Key Laboratory of Cleaner Production of Rare Earths, Ganzhou, 341000, China



ARTICLE INFO

Keywords:
FeCrNiCuTi_x
Ti
High-entropy alloy
Microstructure
Mechanical properties

ABSTRACT

In this study, the microstructural evolution and mechanical properties of a series of FeCrNiCuTi_x ($x = 0, 0.2, 0.4, 0.6, 0.8$, and 1 , in mole ratio) high entropy alloys (HEAs) were analyzed in detail to study the influence of Ti content on the HEAs. The microstructures of the alloys transformed from single-phase face-centered cubic (FCC) phase structure to FCC and body-centered cubic (BCC) diphase, finally to FCC, BCC and intermetallic compound (Fe₂Ti) phase with the increase of Ti content. The addition of Ti element significantly refined the grain of the alloys. The hardness, strength and tribology tests of the alloys were also carried out. The results indicated that the Vickers hardness, yield strength, and fracture strength increased first and then decreased, the average friction coefficient variation law was just the opposite, and the plastic strain reduced monotonically, with the increase of x values for the alloys. At $x = 0.4$, the maximum yield strength and fracture strength of the alloy were 1646.89 MPa and 1947.09 MPa, respectively, and the average friction coefficient was a minimum of 0.47, with a hardness value of HV 489.68 and a plastic strain of 13.98%. The maximum hardness value of the alloy was HV 656.19 at $x = 0.8$. The fracture mechanism of the alloys was from ductile fracture to brittle fracture and the wear mechanism was form of abrasive wear. Accordingly, the FeCrNiCuTi_{0.4} alloy obtained the optimal mechanical properties overall. This research is of great significance for the development of engineering and structural materials with excellent mechanical properties.

1. Introduction

High entropy alloy (HEA) is a new type of alloy developed in recent years, which is composed of five or more main elements, and the atomic fraction of each element is between 5% and 35% [1,2]. The most significant characteristics of HEAs are four core effects: high entropy mixing in the thermodynamics [3], lattice distortion effect in the structure [4], hysteresis diffusion effect in the dynamics [5] and cocktail effect in the performance [6]. These four effects complement each other and work together to make HEA with excellent comprehensive properties. Compared with traditional alloys, the greatest advantage of HEAs is that the properties of HEAs can be controlled by designing the composition of the alloys. As well as the HEA with specific combined properties can be obtained, such as superior hardness [7], superb specific strength

[8], extraordinary wear resistance [9], outstanding corrosion resistance [10], high-temperature resistance [11], and high oxidation resistance [12], etc.

In general, the alloy composition is modulated by changing the content of HEA elements to obtain a specific combination of properties [13–16]. The majority of reported HEAs compositions are based on elements such as Co, Cr, Fe, Ni, Al, Cu, Mn, V, Si, Mo, and Ti [13–16]. For example, Tan et al. [17] investigated that the addition of Si element generated the emergence of a new phase of Cr₃Si in the Co_{0.2}CrAlSi_xNi alloys, which greatly improved the hardness. Stepanov et al. [18] found that adding V element into CoCrFeMnNi can change the alloy microstructure from single face-centered cubic (FCC) phase to FCC and sigma phase diphase structure, and greatly improve the yield strength. Wu et al. [19] studied the wear behaviors of AlCrFeCoNi and

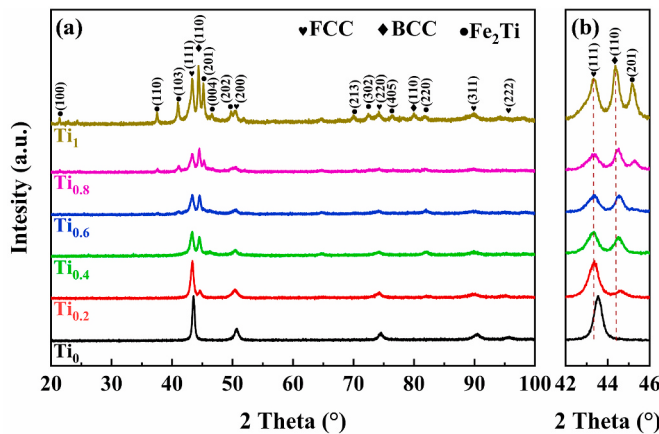
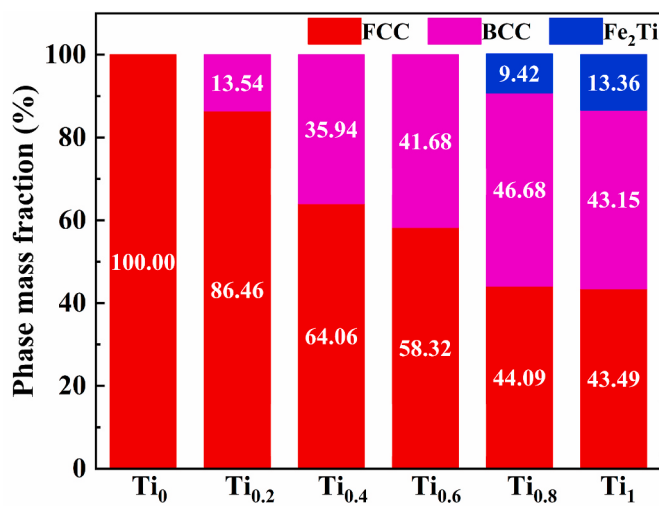
* Corresponding author. Ganjiang Innovation Academy, Chinese Academy of Sciences, Ganzhou, 341000, China.

** Corresponding author. School of Physics and Materials, Nanchang University, Nanchang, 330000, China.

E-mail addresses: lmeng@ipe.ac.cn (L. Meng), tqi@gia.cas.cn (T. Qi).

Table 1Chemical compositions of FeCrNiCuTi_x alloys ($x = 0, 0.2, 0.4, 0.6, 0.8$, and 1).

Alloys	Content/wt. %				
	Fe	Cr	Ni	Cu	Ti
Ti ₀	24.27	22.60	25.51	27.62	0.00
Ti _{0.2}	23.30	21.70	24.49	26.51	4.00
Ti _{0.4}	22.41	20.86	23.55	25.50	7.68
Ti _{0.6}	21.58	20.09	22.68	24.55	11.10
Ti _{0.8}	20.81	19.37	21.87	23.68	14.27
Ti ₁	20.09	18.71	21.11	22.86	17.23

**Fig. 1.** (a) XRD patterns of FeCrNiCuTi_x alloys ($x = 0, 0.2, 0.4, 0.6, 0.8$, and 1); (b) Enlarged patterns from $42\text{--}46^\circ$.**Fig. 2.** Phase mass fraction of FeCrNiCuTi_x alloys ($x = 0, 0.2, 0.4, 0.6, 0.8$, and 1).

AlCrFeCoNiTi_{0.5} HEAs and discovered that doping Ti element increased the hardness and improved the oxidation scale at the same time, which made additional contributions to the wear resistance. At present, many scholars focused on the effect of rare earth elements doping on the mechanical properties of alloys. The hexagonal crystal structure phase will be formed in the alloy by doping of trace rare earth elements and plays a role in refining the grain, thus improving the mechanical properties of the alloy such as hardness and strength [20–23].

Compared with other metallic elements, Ti element has the characteristics of low density and large atomic radius, then doping Ti element into HEAs can significantly reduce the alloy density and enhance the lattice distortion effect to improve the properties of HEAs [24]. Previous

researches have been demonstrated that adding Ti element can improve the mechanical properties of HEAs [19,25,26]. However, most of literatures on HEAs with Ti element have not conducted a comprehensive study on the mechanical properties of the alloy, such as only the strength [25,26], or only the wear resistance [19]. Until now, the influence mechanism of Ti element on mechanical properties has not been clarified. Therefore, it is of great significance to study the effect mechanism of Ti element on the microstructure and mechanical properties.

According to our previous study [27], the high-entropy alloys of Fe–Cr–Ni–Cu–Ti system had excellent corrosion resistance, but the mechanical properties were not clear. In general, Fe and Cr elements can enhance the hardness and strength of the alloy. Ni and Cu elements can enhance the plasticity and improve the toughness of the alloy. It can be inferred that the system alloy has excellent mechanical properties. In this work, the effects of Ti content on the microstructures and mechanical properties of FeCrNiCuTi_x ($x = 0, 0.2, 0.4, 0.6, 0.8$, and 1 , in mole ratio) alloys were investigated, to obtain a high-entropy alloy with excellent comprehensive properties. The research has important guiding significance for the development of high hardness, strong strength and wear resistant alloys, and has greatly expanded and promoted the progress of high entropy alloys in the field of engineering materials.

2. Experimental

2.1. Materials and methods

In this work, bulky or granular Fe, Cr, Ni, Cu, Ti metals with high purity >99.99 wt% were selected as raw materials, according to the molar ration form FeCrNiCuTi_x alloys ($x = 0, 0.2, 0.4, 0.6, 0.8$, and 1) to make the ingredients. Each alloy was abbreviated as Ti₀, Ti_{0.2}, Ti_{0.4}, Ti_{0.6}, Ti_{0.8}, and Ti₁, and the chemical compositions of each alloy were listed in Table 1. A series of FeCrNiCuTi_x alloys were prepared by arc-melting in the argon atmosphere. To ensure chemical homogeneity, each ingot was remelted for ten times. The as-cast ingots were cut into cubic samples with $8\text{ mm} \times 8\text{ mm} \times 1\text{ mm}$ by a wire cutting machine, and the portion was removed to ground into a powder by means of a vibration mill.

2.2. Characterization

The powder samples were detected by X-Ray Diffraction (XRD, D8 ADVANCE, Bruker, Germany) with Cu-K α radiation ($\lambda = 1.5406\text{ \AA}$) to analyze the phase compositions and crystal structures. The XRD was operated at 40 kV and 40 mA with the range of $20\text{--}100^\circ$ and the speed of $2^\circ\cdot\text{min}^{-1}$. After the XRD test, the phase composition was analyzed by the Jade software, and the mass fraction of the phase was analyzed using the Topas software. The cubic samples were grinded and polished, then etched with aqua regia about 12 s . Then, they were characterized via Scanning Electron Microscope with Energy Dispersive Spectroscopy (SEM/EDS, JSM-IT800, JEOL, Japan). After vibration polishing, the analysis was carried out with electron backscatter diffraction (EBSD, AMETEK) and the acceleration voltage was 20 KV . To further analyze the crystal structure and local microstructure, the powder-samples were characterized via the transmission electron microscope (TEM), which operated at 200 kV and equipped with an INCA energy dispersive X-ray spectrometer (EDS) after grinding for 40 h by ball mill.

The theoretical density (D_{theory}) of the alloy was determined by the rule of mixtures according to the equation [28],

$$D_{\text{theory}} = \frac{\sum x_i M_i}{\sum x_i M_i / D_i} \quad (1)$$

where x_i , D_i , and M_i are the atomic fraction, density and atomic mass of the i th element. The experimental density was estimated by the Archimedes principle.

The hardness values of samples were measured by the Vickers

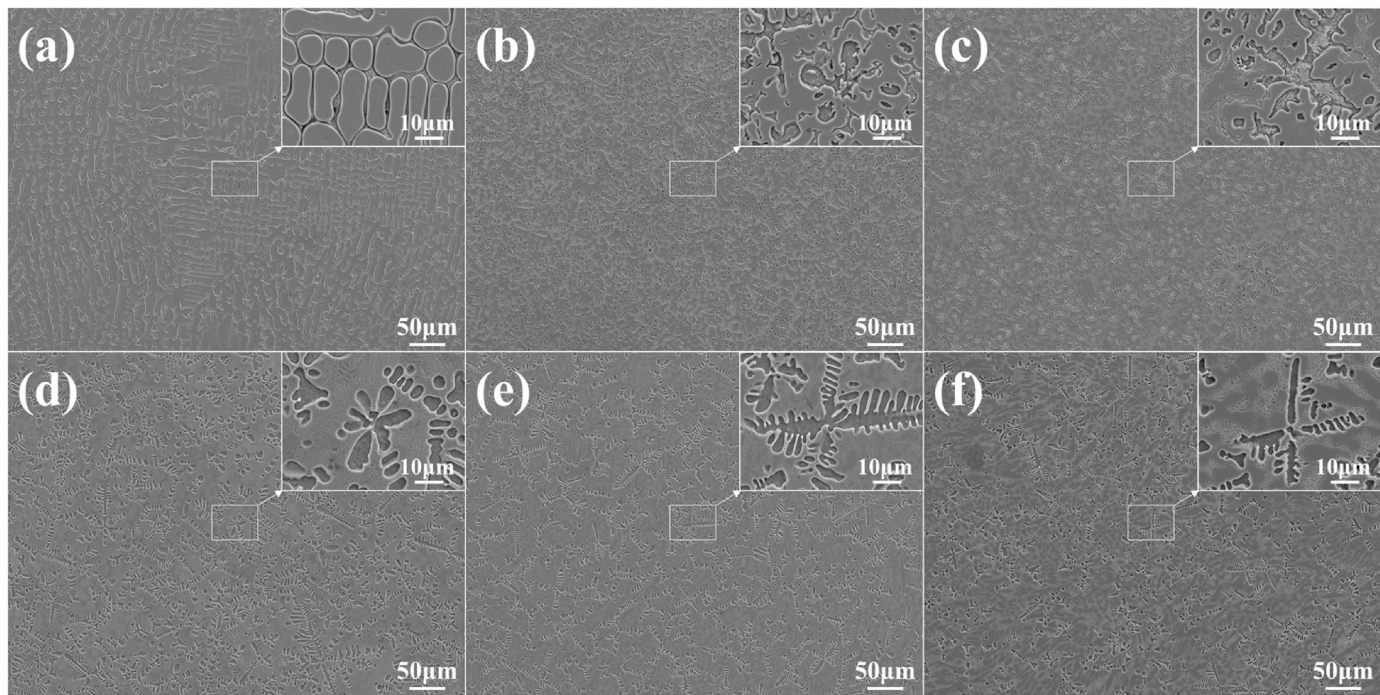


Fig. 3. SEM micrographs of FeCrNiCuTi_x alloys ($x = 0, 0.2, 0.4, 0.6, 0.8$, and 1); (a) Ti₀, (b) Ti_{0.2}, (c) Ti_{0.4}, (d) Ti_{0.6}, (e) Ti_{0.8}, (f) Ti₁.

hardness tester (TMVP-1, ShiDai, China). The loading load and time were 4.9 N and 15 s, respectively. The nine points were selected for the hardness tests and the final hardness was the average value after removing the maximum and minimum values.

The nanoindentation test was performed on the Nano indenter (Anton Paar UNHT, Austria) with a load of 10 mN and a loading rate of 20 mN min⁻¹. The displacement (depth) of the indenter was continuously monitored and the load-displacement (P-h) curve was drawn. In order to ensure the accuracy of measurement results, more than three tests were performed for each condition.

The strength tests were performed using an INSTRON-5982 materials testing machine at a strain rate of 1×10^{-3} s⁻¹. The cylindrical specimens with the size of 5 mm in diameter and 10 mm in length were cut for the room-temperature compression tests. The dog-bone-shaped tensile specimens had a gauge section of 20 mm (l) \times 2 mm (w) \times 2 mm (t) for the room-temperature tensile tests. To ensure the accuracy of the experiment, three sets of samples were prepared for each test.

The wear resistance of the alloys was evaluated in a room environment via a friction wear testing machine (HT-1000, LanZhouZhongKe-KaiHua, China). The wear tests were performed at a sliding velocity of 0.98 rad s⁻¹ along a circular path of 6 mm in diameter under a normal load of 10 N, and the sliding distance was 1.764 m. The pin was a silicon nitride (Si₃N₄) ball with a diameter of 6 mm. For each test, a fresh Si₃N₄ ball was used to ensure that all tests were carried out under the same condition. The weight before or after friction test was measured using an FB224 electronic balance with an accuracy of ± 0.1 mg. For each specimen, at least three measurements were performed to ensure the accuracy of the data.

3. Results and discussion

3.1. Phase and microstructure of FeCrNiCuTi_x alloys

The X-ray diffraction patterns of FeCrNiCuTi_x alloys ($x = 0, 0.2, 0.4, 0.6, 0.8$, and 1) alloys were displayed in Fig. 1. The crystal structure of Ti₀ alloy was the single face-centered cubic (FCC) phase. After the addition of Ti element, the body-centered cubic (BCC) phase appeared. The addition of Ti element promoted the formation of BCC phase [29].

When the mole ratio of Ti element attached 0.8, the Fe₂Ti phase emerged, which was similar to the related research [30]. According to Jade software analysis, the space group of Fe₂Ti intermetallic compound was P63mmc(194), which was a kind of the hexagonal close-packed (HCP) phase. According to previous research [31], the single-phase FCC solid solution high-entropy alloy showed good plasticity, and the single-phase BCC solid solution alloy displayed high hardness. From the amplification of XRD pattern (Fig. 1(b)), it can be found that the position of the characteristic diffraction peaks of FCC and BCC phase shifted to a small angle with the increase of Ti content. Due to the large atomic radius of Ti element, the addition of Ti element may enhance the lattice distortion effect of the alloy, thus improving the lattice constant of the alloy.

Fig. 2 showed the mass fraction of different phases in alloys as determined by software analysis. As observed, the BCC phase mass fraction first increased and then decreased, and the FCC phase mass fraction always decreased with the addition of Ti content. The highest BCC phase content of Ti_{0.8} alloy was 46.68%, while the lowest FCC phase content of Ti₁ alloy was 43.49%. From this result, it was inferred that Ti_{0.8} alloy had the highest hardness. In addition, The Fe₂Ti phase content of Ti_{0.6} alloy was less than 5% by software analysis, which was generally negligible.

Fig. 3 revealed the microstructures of FeCrNiCuTi_x alloys ($x = 0, 0.2, 0.4, 0.6, 0.8$, and 1). Fig. 4 exhibited the EDS mapping images in the white box enlarged in Fig. 3. Areas (a), (b), (c), (d), (e) and (f) were enlarged views of the morphology of HEAs, respectively. Several points in the SEM micrographs were selected and measured the element contents by EDS, as listed in Table 2. The Ti₀ alloy was the single FCC phase structure with the average grain size of ~ 100 μ m, which had dendrite (DR) and interdendrite (ID) morphology, as shown in Fig. 3(a). After the addition of Ti element, a petal-like new phase was precipitated in the inner part of the dendrite. The grain of alloys was obviously refined with the addition of Ti element. As shown in Fig. 4, the petal-like new phase can be easily identified as the Cr-rich BCC phase. With the augment of Ti content, the volume fraction of the petal-like new phase first increased and then reduced, which was consistent with the XRD analysis results (Fig. 1). In all alloys, it can be seen that Cu element was enriched at grain boundaries due to its high molar mixing enthalpy, which was similar to

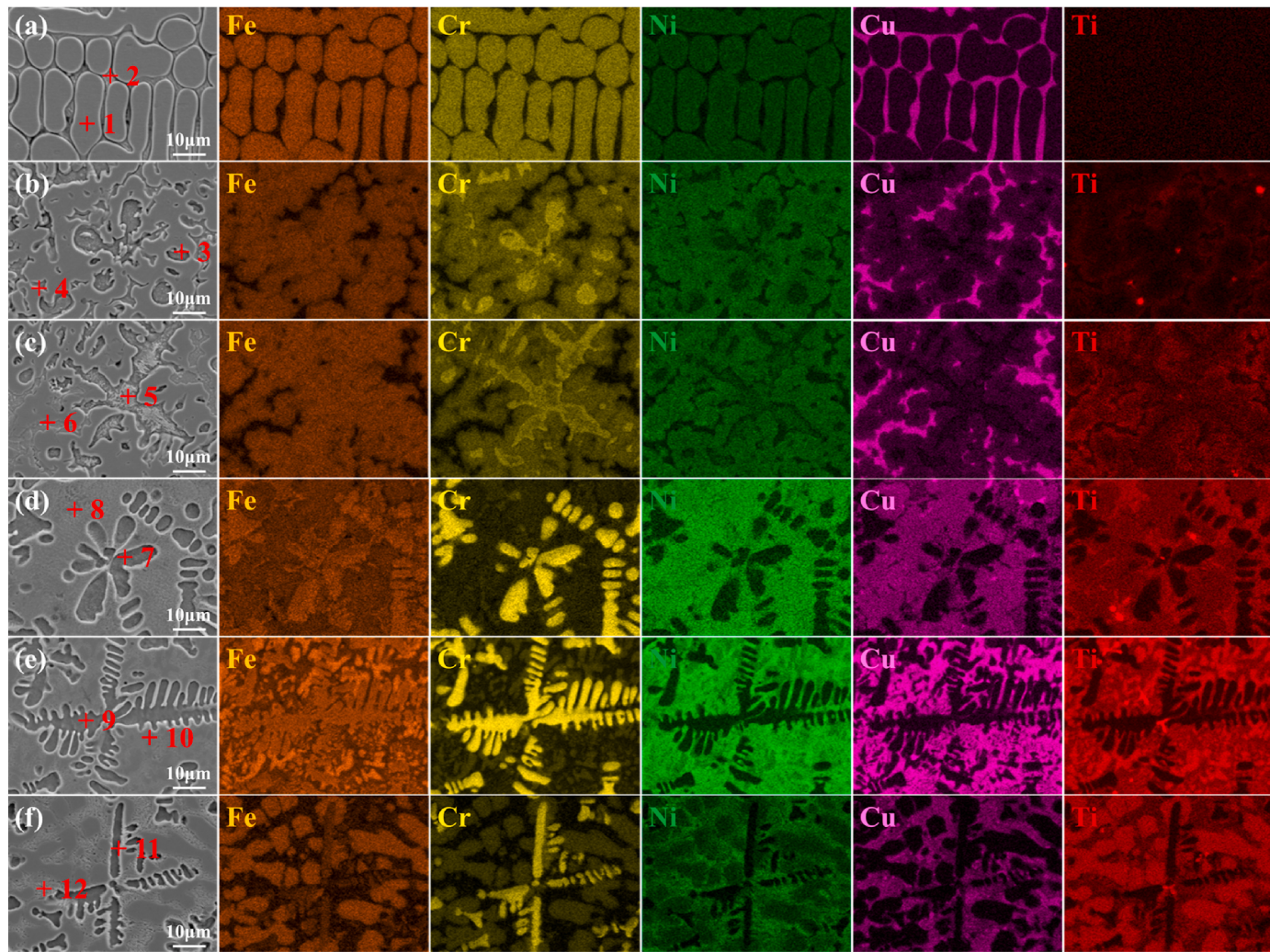


Fig. 4. EDS mapping images of FeCrNiCuTi_x alloys ($x = 0, 0.2, 0.4, 0.6, 0.8$, and 1); (a) Ti_0 , (b) $\text{Ti}_{0.2}$, (c) $\text{Ti}_{0.4}$, (d) $\text{Ti}_{0.6}$, (e) $\text{Ti}_{0.8}$, (f) Ti_1 .

the previous study [32]. The enthalpy of mixing values for Cu and Fe, Cr, Ni, and Ti are $13, 12, 4$ and -9 kJ mol^{-1} , respectively [33], which do not balance the entropy of mixing of the alloys. However, pure Cu has good ductility and is often added to alloys to ensure that it has sufficient plasticity [34]. The Fe, Ni, and Ti elements were abundant in the dendrite, and Cr element was enriched in petal-like grains.

To better reveal the phase content and grain size of the alloys, Ti_0 and $\text{Ti}_{0.4}$ alloys were selected for EBSD characterization, and the results were illustrated in Fig. 5. According to the phase distribution maps (Fig. 5(a) and (b)), the FCC phase content of $\text{Ti}_{0.4}$ alloy was 65.59%, and the BCC phase content was 34.41%, which was similar to the XRD analysis results (Fig. 2). From Fig. 5(c) and (d), the average grain sizes of Ti_0 and $\text{Ti}_{0.4}$ alloys were 110.7 and $3.4 \mu\text{m}$, respectively. The results indicated that the grain size of the alloy was greatly reduced after adding Ti element with a molar ratio of 0.4, which was consistent with the SEM analysis results (Fig. 3). Adding Ti element to the alloys can improve the nucleation rate, and prevent grain growth and grain boundary movement, and refine the grains. This may be the addition of Ti element could reduce the surface tension of phase interface and the energy fluctuation of nucleation according to the classical nucleation theory [35].

The powder samples were analyzed by HR-TEM with EDS, to further understand the microstructure of FeCrNiCuTi_x alloys ($x = 0, 0.2, 0.4, 0.6, 0.8$, and 1). Took Ti_0 and $\text{Ti}_{0.4}$ alloys for examples, and the results were presented in Figs. 6 and 7, respectively. The typical selected area electron diffraction (SAED) pattern of Ti_0 alloy was indicated in Fig. 6

(a). The single-phase FCC structure of Ti_0 alloy could be determined using the calibration of the diffraction ring, which fully verified the results of the XRD analysis. The fast Fourier transform (FFT) and inverse Fourier transform were applied to the HR-TEM image of the red box area in Fig. 6(c), and the phase crystal plane spacing in this area was 0.2126 nm , thus it can be deduced that the red box area may be the (1 1 1) plane of the FCC phase. From Fig. 6(d), Fe, Cr, Ni and Cu elements were equally evenly distributed in the alloy, and there was no element segregation. In addition to the existence of the FCC phase structure in $\text{Ti}_{0.4}$ alloy, there may also be another phase through the calibration of the diffraction ring in Fig. 7(a), which was most likely Cr-rich BCC phase. The grain surface spacing in Fig. 7(c) was close to 0.2113 nm , from which it can be inferred that the region A in Fig. 7(b) may be the (1 1 1) face of the FCC phase. Likewise, the (1 1 0) plane of the BCC phase was identified. According to Fig. 7(e), the EDS mapping revealed that there was a small amount of Cr element segregation of the alloy, indicating the formation of Cr-rich phase.

3.2. Mechanical properties of FeCrNiCuTi_x alloys

3.2.1. Density

The theoretical density by formula (1) and measured Archimedes density of the FeCrNiCuTi_x alloys ($x = 0, 0.2, 0.4, 0.6, 0.8$, and 1) were summarized in Table 3. It could be seen that the alloy density decreased with the increase of Ti element content, because Ti element had the

Table 2
Components of each test point and area in Fig. 4.

Alloys	Region	Atom percent/wt. %				
		Fe	Cr	Ni	Cu	Ti
Ti ₀	(a)	25.08 ± 0.04	25.11 ± 0.04	26.36 ± 0.05	23.45 ± 0.05	—
		30.62 ± 0.17	29.15 ± 0.15	28.36 ± 0.18	11.87 ± 0.17	—
	1	7.95 ± 0.10	8.09 ± 0.09	12.63 ± 0.09	71.33 ± 0.14	—
		0.10	0.09	0.14	0.18	—
	(b)	24.67 ± 0.04	23.09 ± 0.04	27.2 ± 0.05	20.26 ± 0.05	4.78 ± 0.02
		31.61 ± 0.17	42.25 ± 0.18	17.90 ± 0.17	5.99 ± 0.15	2.26 ± 0.06
	(c)	4.50 ± 0.09	3.66 ± 0.07	11.75 ± 0.15	77.35 ± 0.15	2.74 ± 0.06
		23.96 ± 0.04	21.88 ± 0.04	24.56 ± 0.05	22.05 ± 0.05	7.55 ± 0.02
	(d)	27.32 ± 0.16	28.01 ± 0.15	28.86 ± 0.19	8.98 ± 0.19	6.82 ± 0.08
		3.64 ± 0.08	2.49 ± 0.07	10.27 ± 0.07	80.34 ± 0.14	3.27 ± 0.07
	(e)	22.51 ± 0.04	17.18 ± 0.03	27.71 ± 0.05	22.48 ± 0.05	10.12 ± 0.03
		28.39 ± 0.16	50.73 ± 0.18	12.53 ± 0.15	3.57 ± 0.13	4.79 ± 0.07
	(f)	16.19 ± 0.13	6.68 ± 0.09	33.75 ± 0.19	30.08 ± 0.19	13.29 ± 0.10
		20.94 ± 0.02	23.25 ± 0.02	21.38 ± 0.03	20.06 ± 0.03	14.37 ± 0.02
	(g)	24.4 ± 0.15	62.59 ± 0.18	6.76 ± 0.12	2.48 ± 0.12	3.77 ± 0.06
		12.68 ± 0.12	5.54 ± 0.08	27.29 ± 0.18	41.27 ± 0.21	13.23 ± 0.11
	(h)	19.95 ± 0.04	18.20 ± 0.04	22.5 ± 0.05	20.70 ± 0.05	18.65 ± 0.03
		21.90 ± 0.15	65.99 ± 0.19	4.84 ± 0.12	2.78 ± 0.12	4.50 ± 0.06
	(i)	6.70 ± 0.10	2.46 ± 0.07	36.09 ± 0.20	39.07 ± 0.21	15.67 ± 0.11

smallest density compared with other elements in the FeCrNiCuTi_x alloys. The theoretical density of the alloys lied in the range of 7.19–8.21 g cm⁻³. Also, the measured Archimedes density of the alloys were between 7.04–8.09 g cm⁻³. The theoretical density of each alloy was consistent with the measured density.

3.2.2. Vickers hardness

Fig. 8 displayed the Vickers hardness and BCC phase mass fraction of FeCrNiCuTi_x alloys ($x = 0, 0.2, 0.4, 0.6, 0.8$, and 1). With increasing the Ti content, Vickers hardness and BCC phase content of alloys first increased sharply, then gently increased and finally slowly decreased, reaching the highest value at $x = 0.8$. Vickers hardness values and BCC phase mass fraction of alloys were listed in Table 4. As the molar ratio of Ti element boosted from 0 to 8, Vickers hardness values furthered from a minimum of HV 154.79 ± 1.12 (Ti₀ alloy) to a maximum of HV 656.19 ± 8.10 (Ti_{0.8} alloy) and BCC phase mass fraction raised from 0 to 46.68% (maximum value). It can be found that the hardness was positively correlated with the mass fraction of BCC phase. Roughly, the relationship between Vickers hardness and BCC phase mass fraction can be expressed as HV = 10.437379 M_{BCC} + 162.7614574, where HV and M_{BCC} were the value of Vickers hardness and mass fraction of BCC phase (%), respectively.

On the one hand, the increase of mass fraction of hard BCC phase can result in the increase of Vickers hardness. As manifested by the previous studies [36,37], the increment of the hardness was attributed to the precipitation of a large number BCC phase. On the other hand, the grain refinement of the alloy resulted in grain boundary strengthening [38], which led to the increase of hardness value of the alloy. The grain size of Ti₀ alloy was significantly larger than other alloys, which was part of the reason for the minimum hardness of the alloy. The Fe₂Ti phase, as an

intermetallic compound, had a negative effect on the hardness of the alloy, which can be confirmed by increasing the x value from 0.8 to 1, increasing the Fe₂Ti phase mass fraction in the alloy from 9.42% to 13.36%, but decreasing the alloy hardness from HV 656.19 to HV 616.65.

3.2.3. Nano-mechanical properties

The nanoindentation method is a simple and effective method to study the nanomechanical properties and deformation behavior of small-volume materials, such as small grains with different grain orientations and single phases [39]. Fig. 9 presented the typical nanoindentation P-h curves of the FCC, BCC and Fe₂Ti phases in Ti₁ alloy. As shown in Fig. 9, it can be seen that the maximum penetration depth of BCC phase was smaller than those of FCC and Fe₂Ti phases under the same load, indicating that BCC phase had stronger plastic deformation resistance. The corresponding nanohardness (H) and elastic modulus (E) values were obtained from the curves on the Oliver-Pharr method and shown in Table 5. For the Ti₁ alloy, the H of FCC, BCC and Fe₂Ti phases were 5.525, 12.033 and 9.363 GPa, respectively, while the E of FCC, BCC and Fe₂Ti phases were 197.444, 222.079 and 212.188 GPa, respectively. The nanohardness and elastic modulus of BCC phase were much higher than those of FCC phase and slightly higher than those of Fe₂Ti phase. The precipitation of BCC phase was the main factor improving the Vickers hardness, and the content of BCC phase was positively correlated with the hardness value of the alloy.

3.2.4. Compressive strength

The engineering stress-strain curves of FeCrNiCuTi_x alloys ($x = 0, 0.2, 0.4, 0.6, 0.8$, and 1) were obtained by compression measurements, as depicted in Fig. 10, and Table 6 listed the summary of compressive yield strength σ_y , fracture strength σ_f and plastic strain ε_p with the content of Ti element. After doping Ti element, the alloys became brittle, especially for Ti_{0.6}, Ti_{0.8}, and Ti₁ alloys. Obviously, the yield strength of alloys was significantly related to Ti content. The yield strength of Ti₀ alloy was appropriately 259.03 MPa, with high work hardening ability, and the compression height reduced by 80% without breaking. Accompanied by the increase of x value for FeCrNiCuTi_x alloys, the yield strength and fracture strength first increased then decreased, while the plastic strain kept reducing. Ti_{0.4} alloy exhibited maximum compressive strength (1646.89 MPa) and fracture strength (1947.09 MPa). The compressive strength of Ti_{0.4} alloy was greater than those of CoCrCu-FeNiTi_{0.5} alloy (1650 MPa) [25] and CoCrFeNiTi_{0.3} alloy (1529 MPa) [26], so it has great potential application prospects as an engineering material.

By increasing Ti element content of the largest radius atom in FeCrNiCuTi_x alloys, the movement of atoms in the alloy was inhibited, thus triggering the solid solution strengthening and pinning effect [40], so as to optimize the mechanical properties of the alloys. Meantime, the second phase strengthening effect caused by the precipitation of BCC phase would also enhance the strength of the alloy. As the value of x varied from 0 to 0.4, the strength increase might be caused by the strengthening effect of solid solution and second phase. However, when $x \geq 0.4$, the strength of the alloys reduced with the increase of Ti content, which may be because the independent presence of BCC phase broke up the phase continuity in the alloy. Combined with SEM-EDS analysis in Fig. 4, the addition of Ti element induced the formation of Cr-rich BCC phase. When $x \leq 0.4$, the BCC phase grew out in FCC phase, while BCC phase was enriched in the FCC phase boundary at $x > 0.4$, thus breaking the phase continuity in the alloy. The splitting effect [41] caused by the Cr-rich BCC phase reduced the strength of Ti_{0.6} alloy. For Ti_{0.8} and Ti₁ alloys, the formation of intermetallic compound Fe₂Ti phase worsened their mechanical properties by a step.

The change of composition caused by the microstructure evolution not only affected the mechanical properties of HEAs, but also changed the fracture behavior, as shown for the fracture morphology of FeCr-NiCuTi_x alloys ($x = 0.2, 0.4, 0.6, 0.8$, and 1) presented in Fig. 11 after

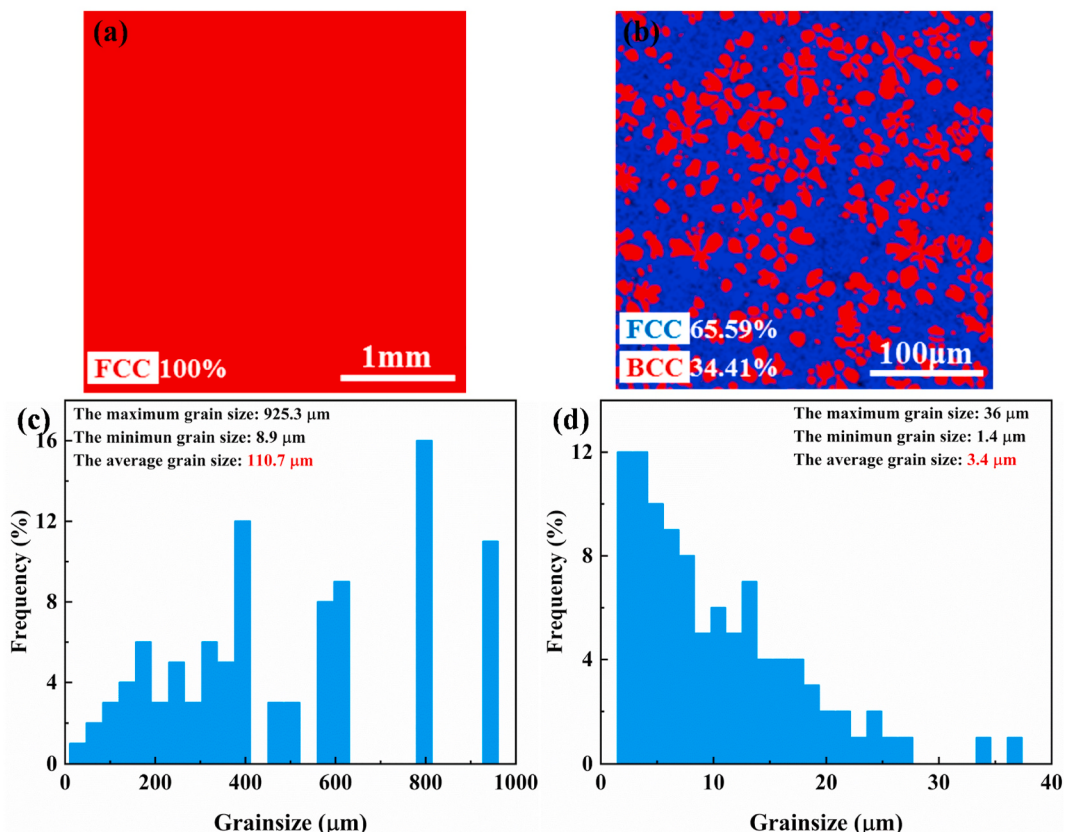


Fig. 5. EBSD results of Ti_0 and $\text{Ti}_{0.4}$ alloys; (a) the phase distribution map of Ti_0 alloy, (b) the phase distribution map of $\text{Ti}_{0.4}$ alloy, (c) the grain size distribution derived from the results in (a), (d) the grain size distribution derived from the results in (b).

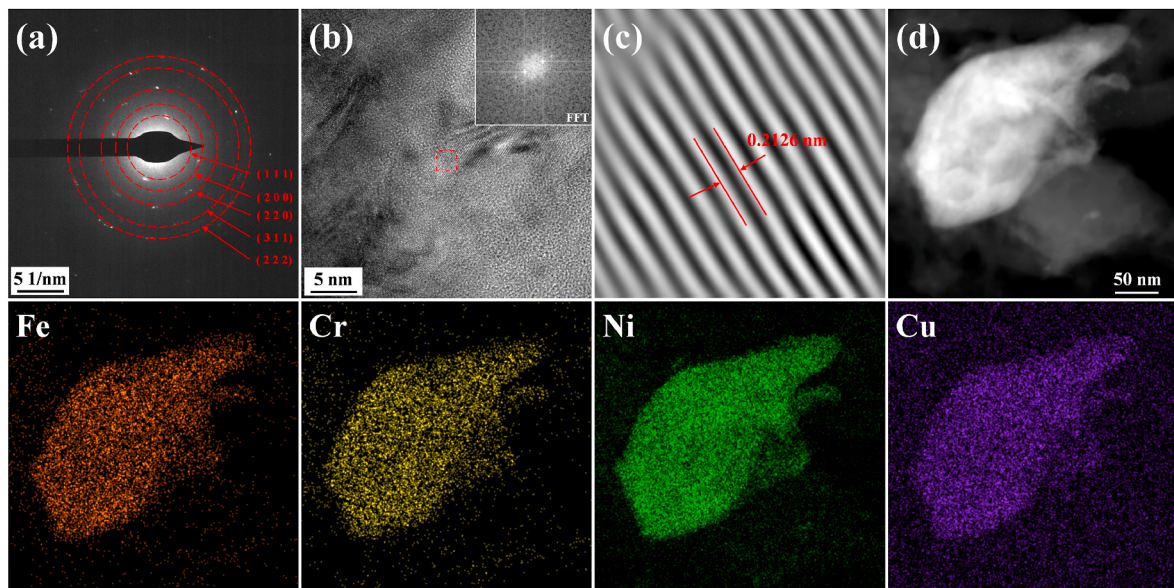


Fig. 6. TEM-EDS maps of Ti_0 alloy; (a) SAED pattern of Ti_0 alloy, (b) HR-TEM image and FFT pattern of the red box area, (c) the inverse FFT pattern of the red box area; (d) EDS mapping of Ti_0 alloy. (For interpretation of the references to colour in this figure legend, the reader is referred to the Web version of this article.)

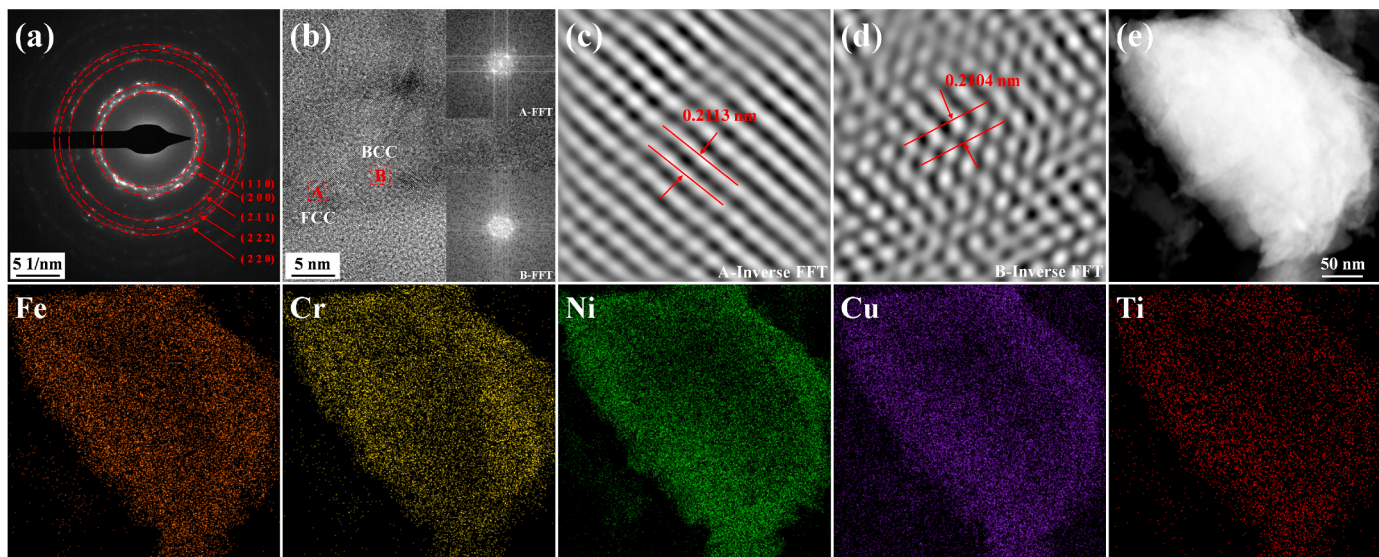


Fig. 7. TEM-EDS maps of $\text{Ti}_{0.4}$ alloy; (a) SAED pattern of $\text{Ti}_{0.4}$ alloy, (b) HR-TEM image and FFT pattern of region A and B, (c) the inverse FFT pattern of region A, (d) the inverse FFT pattern of region B, (e) EDS mapping of $\text{Ti}_{0.4}$ alloy.

Table 3

Theoretical density and measured Archimedes density of FeCrNiCuTi_x alloys ($x = 0, 0.2, 0.4, 0.6, 0.8$, and 1).

Alloys	Ti_0	$\text{Ti}_{0.2}$	$\text{Ti}_{0.4}$	$\text{Ti}_{0.6}$	$\text{Ti}_{0.8}$	Ti_1
Theoretical density/ $\text{g}\cdot\text{cm}^{-3}$	8.21	7.95	7.72	7.52	7.35	7.19
Measured Archimedes density/ $\text{g}\cdot\text{cm}^{-3}$	8.09	7.76	7.64	7.31	7.24	7.04

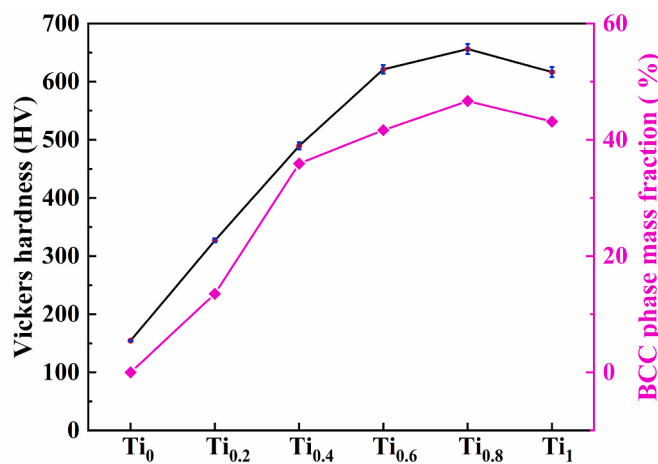


Fig. 8. Vickers hardness and BCC mass phase fraction of FeCrNiCuTi_x alloys ($x = 0, 0.2, 0.4, 0.6, 0.8$, and 1).

compression tests. For $\text{Ti}_{0.2}$, $\text{Ti}_{0.4}$, and $\text{Ti}_{0.6}$ alloys (Fig. 11(a), (d), and (c)), a large number of dimples appeared on the fracture surface, display typical ductile fractures. It can be seen from Fig. 11(d) and (e) that some cleavage steps, rock candy cracks and tear edges occurred on the fracture surface of $\text{Ti}_{0.8}$, and Ti_1 alloys, which were typical brittle fracture characteristics. To sum up, the fracture mode of the alloys transformed

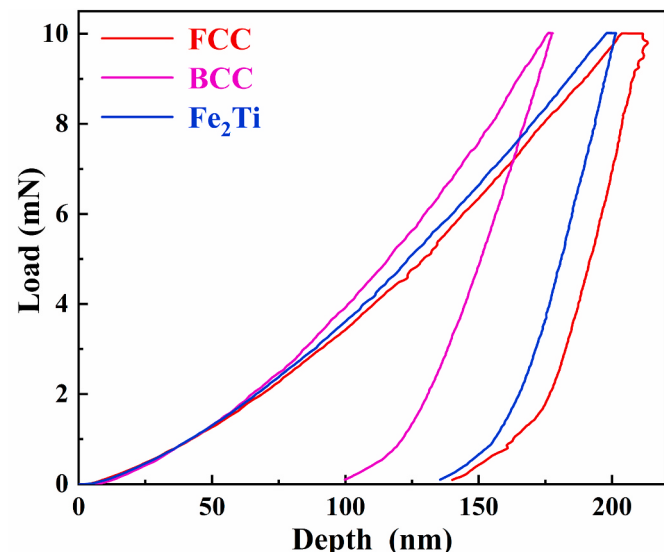


Fig. 9. Typical nanoindentation P-h curves within the FCC, BCC and Fe_2Ti phases in FeCrNiCuTi alloy.

from ductile fracture to brittle fracture along with the increase of Ti content.

3.2.5. Tensile strength

The engineering stress-strain curves of FeCrNiCuTi_x alloys ($x = 0, 0.2, 0.4, 0.6, 0.8$, and 1) were obtained through tensile tests, as described in Fig. 12. The variation laws of tensile yield strength σ_y , fracture strength σ_f and plastic strain ε_p with the content of Ti element were shown in Table 7. It can be seen the tensile stress-strain curve was extremely unsMOOTH, which was unreasonable very much. According to the phase analysis, Ti_0 alloy should have the best ductility, but the test

Table 4

Vickers hardness and BBC phase mass fraction of FeCrNiCuTi_x alloys ($x = 0, 0.2, 0.4, 0.6, 0.8$, and 1).

Alloys	Ti_0	$\text{Ti}_{0.2}$	$\text{Ti}_{0.4}$	$\text{Ti}_{0.6}$	$\text{Ti}_{0.8}$	Ti_1
Hardness/HV	154.79 ± 1.12	327.01 ± 3.38	489.68 ± 5.72	621.31 ± 6.82	656.19 ± 8.10	616.65 ± 8.28
Mass fraction/%	0	13.54	35.94	41.68	46.68	43.15

Table 5

Nanohardness (H) and elastic modulus (E) of the FCC, BCC and Fe₂Ti phases.

Phase	FCC	BCC	Fe ₂ Ti
H/GPa	5.525	12.033	9.363
E/GPa	197.444	222.079	212.188

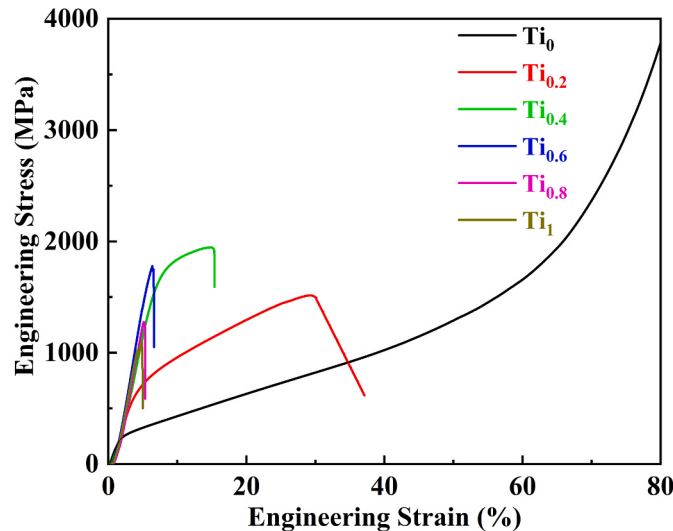


Fig. 10. Compressive engineering stress-strain curves of FeCrNiCuTi_x alloys ($x = 0, 0.2, 0.4, 0.6, 0.8$, and 1).

Table 6

Summary of compression yield strength (σ_y), fracture strength (σ_f), and plastic strain (ϵ_p) of FeCrNiCuTi_x alloys ($x = 0, 0.2, 0.4, 0.6, 0.8$, and 1).

Alloys	σ_y /MPa	σ_f /MPa	ϵ_p %
Ti ₀	259.03	Not fractured	>80
Ti _{0.2}	523.36	1515.67	28.41
Ti _{0.4}	1646.89	1947.09	13.98
Ti _{0.6}	1626.67	1778.85	5.25
Ti _{0.8}	1266.75	1276.27	3.77
Ti ₁	966.66	1092.58	3.76

results were not satisfactory. It can be seen from Table 7 that the maximum plastic strain was 2.99% (Ti_{0.6} alloy) and the minimum was 0.14% (Ti_{0.2} alloy). Ti₀ alloy had high plastic strain (2.10%) in the alloys. The tensile strength of the alloy was too low to match the actual results, especially for Ti_{0.8} alloy. Due to the large size of samples prepared, defects such as micro-pore and voids will inevitably appear by the vacuum arc melting [42]. It may be the main reason for the unsatisfactory lifting results.

3.2.6. Tribology

Fig. 13 demonstrated the evolution of friction coefficient vs. sliding time for FeCrNiCuTi_x alloys ($x = 0, 0.2, 0.4, 0.6, 0.8$, and 1) at room temperature, which was roughly divided into two stages [43]: running-in stage before 4 min, where the friction coefficient gradually increased and tended to be stable; After that, there was a stable period, and the curve of friction coefficient was balanced and stable, showing periodic fluctuations. The average friction coefficient and friction loss quantity of FeCrNiCuTi_x alloys ($x = 0, 0.2, 0.4, 0.6, 0.8$, and 1) were listed in Table 8. The average friction coefficient of Ti₀ alloy was 0.72. Obviously, the average friction coefficient of the alloy was significantly reduced after adding Ti element. When $x = 0.4$, the average friction coefficient of the alloy reached the minimum value of 0.47. At $x \geq 0.4$, the wear quality of alloys decreased significantly with less than or equal

to 0.7 mg. The wear rate of the alloy can be based on the formula (2),

$$W_r = \Delta V / (L \cdot F) \quad (2)$$

where W_r , ΔV , L and F are the wear rate of the alloy, the volume wear of the material, the total sliding distance of the dual ball during friction and the load applied to the surface of the sample. Among, the ΔV can be calculated by the density formula, $L = 1.764$ m and $F = 10$ N according to the experimental conditions. The calculation results were also presented in Table 8. Similarly, the wear rate of the alloy was significantly reduced after adding Ti element. At $x \geq 0.2$, the wear rate was reduced by an order of magnitude to the order of 10^{-6} , so there was not much difference between them. These results represented that the wear resistance of the alloy had been greatly improved. In general, the alloys with high strength and hardness exhibit good wear resistance [44]. Ti_{0.4} alloy had the highest strength and strong hardness, thus manifesting the optimum wear resistance.

The SEM images of worn surfaces of FeCrNiCuTi_x alloys ($x = 0, 0.2, 0.4, 0.6, 0.8$, and 1) were displayed in Fig. 14. It can be seen that a large number of furrows and abrasive chips were distributed along the sliding direction of the abrasive surface of the alloy. The wear characteristics of alloys wear surface, such as furrow and wear chips, were mainly caused by the continuous ploughing of the dual Si₃N₄ ball during the friction process, which was a typical wear particle wear form. The wear marks on the surface of Ti₀ alloy were wide and deep. After the incorporation of Ti element, the wear traces became significantly narrower and shallower, and the wear chips were decreased, further indicating that the wear resistance of the alloy had been improved.

4. Conclusions

In this study, the effects of doping Ti element on the microstructures and mechanical properties of FeCrNiCuTi_x high entropy alloys were examined in as-cast condition. The main conclusions were as follows:

- (1) By adding Ti element to the alloy, the alloy transformed a single FCC phase structure to a FCC and BCC diphase structure, and the grains were significantly refined, with grain sizes changing from 110.7 μ m in Ti₀ alloy to 3.4 μ m in Ti_{0.4} alloy. With the further increase of Ti content, a new phase - intermetallic compound Fe₂Ti phase appeared in Ti_{0.8} and Ti₁ alloys.
- (2) The addition of Ti enhanced Vickers hardness of the alloy, and hardness was positively correlated with the mass fraction of BCC phase. As the molar ratio of Ti increased from 0 to 1, the hardness of the alloy increased from HV154.79 to HV616.65, and BCC phase content changed from 0 to 43.15%, respectively. The maximum hardness of Ti_{0.8} alloy was HV 656.19 and BCC phase content was 46.68%, respectively. The maximum nanohardness and elastic modulus of BCC phase were 12.033 and 222.079 GPa in FeCrNiCuTi alloy, respectively.
- (3) As x increased, the yield strength of alloys improved from 259.03 MPa (Ti₀ alloy) to 1646.89 MPa (Ti_{0.4} alloy) and then reduced to 966.66 MPa (Ti₁ alloy). When $x = 0.4$, the highest yield strength of the alloy was 1646.89 MPa, the fracture strength was 1947.09 MPa and the plastic strain was 13.98%. The strengthening mechanism included solid-solution strengthening and second phase strengthening. The fracture mode of the alloy transformed from ductile fracture to brittle fracture. The increase in Ti element was the main reason for the transition of alloy fracture mechanism from ductile fracture to brittle fracture.
- (4) The increase in Ti content not only enhanced the hardness and strength of the alloy, but also significantly improved the wear resistance. The average friction coefficient and wear rate of the alloy were greatly reduced after adding Ti element. At $x = 0.4$, the wear resistance of the alloy was the most prominent, with the lowest average friction coefficient of 0.47 and lower wear rate of

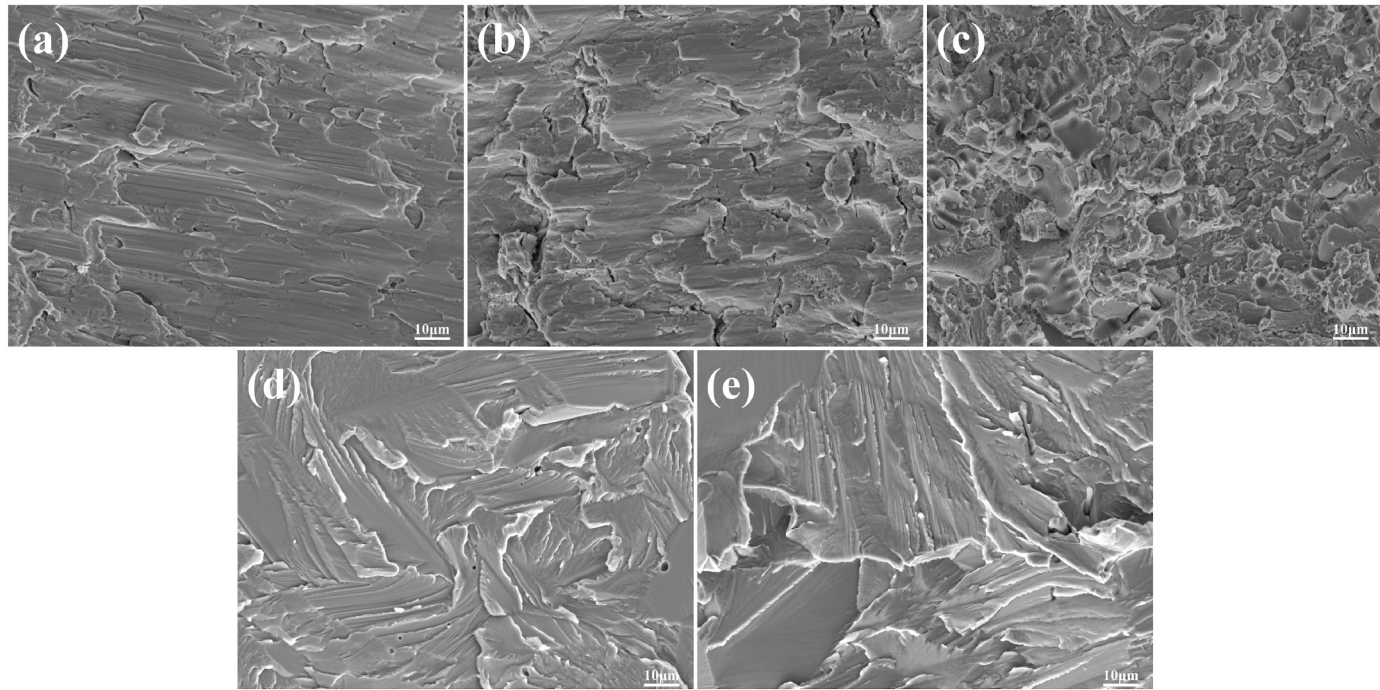


Fig. 11. Fracture surface morphology of FeCrNiCuTi_x alloys ($x = 0.2, 0.4, 0.6, 0.8$, and 1); (a) $\text{Ti}_{0.2}$, (b) $\text{Ti}_{0.4}$, (c) $\text{Ti}_{0.6}$, (d) $\text{Ti}_{0.8}$, (e) Ti_1 .

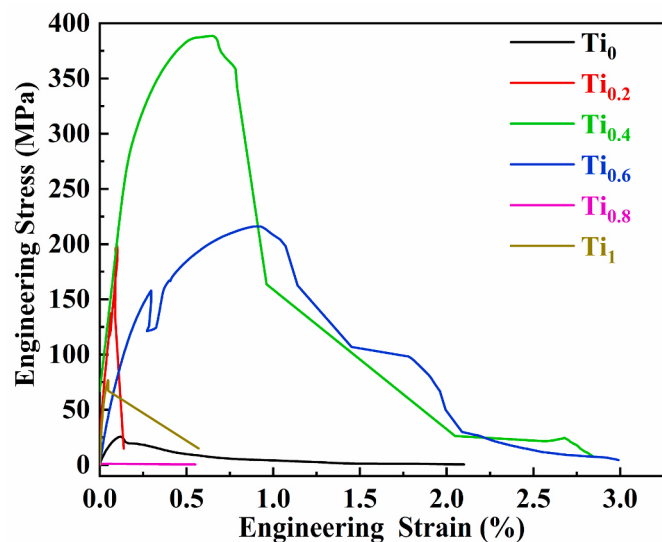


Fig. 12. Tensile engineering stress-strain curves of FeCrNiCuTi_x alloys ($x = 0, 0.2, 0.4, 0.6, 0.8$, and 1).

Table 7

Variation laws of tensile yield strength (σ_y), fracture strength (σ_f), and plastic strain (ε_p) of FeCrNiCuTi_x alloys ($x = 0, 0.2, 0.4, 0.6, 0.8$, and 1).

Alloys	σ_y/MPa	σ_f/MPa	$\varepsilon_p/\%$
Ti_0	18.18	25.66	2.10
$\text{Ti}_{0.2}$	192.36	198.94	0.14
$\text{Ti}_{0.4}$	371.68	388.61	2.84
$\text{Ti}_{0.6}$	121.31	216.18	2.99
$\text{Ti}_{0.8}$	0.87	1.15	0.55
Ti_1	38.08	145.70	0.27

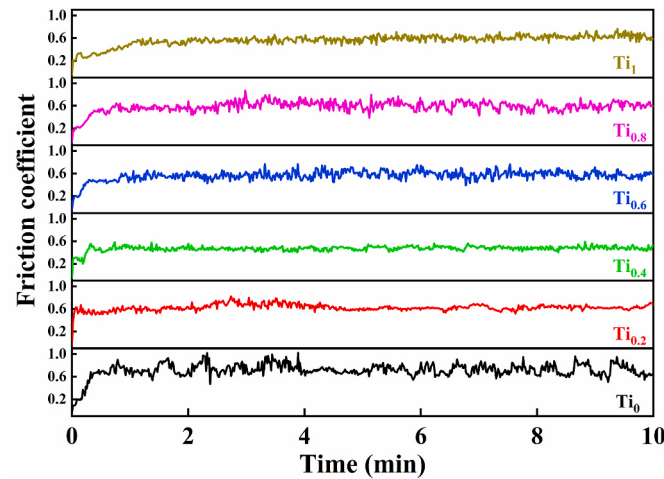


Fig. 13. Evolution of friction coefficient vs. sliding time for FeCrNiCuTi_x alloys ($x = 0, 0.2, 0.4, 0.6, 0.8$, and 1).

Table 8

Average friction coefficient, friction loss quantity and wear rate of FeCrNiCuTi_x alloys ($x = 0, 0.2, 0.4, 0.6, 0.8$, and 1).

Alloys	Ti_0	$\text{Ti}_{0.2}$	$\text{Ti}_{0.4}$	$\text{Ti}_{0.6}$	$\text{Ti}_{0.8}$	Ti_1
Average friction coefficient	0.72	0.62	0.47	0.56	0.59	0.56
Friction loss quantity/mg	3.1	1.3	0.7	0.5	0.6	0.5
Wear rate/ $10^{-6} \text{ mm}^3 \text{ N}^{-1} \text{ m}^{-1}$	21.73	9.50	5.20	3.88	4.70	4.02

$5.20 \times 10^{-6} \text{ mm}^3 \text{ N}^{-1} \text{ m}^{-1}$. The wear mechanism of the alloy was a typical form of particle wear.

Declaration of competing interest

The authors declare that they have no known competing financial interests or personal relationships that could have appeared to influence the work reported in this paper.

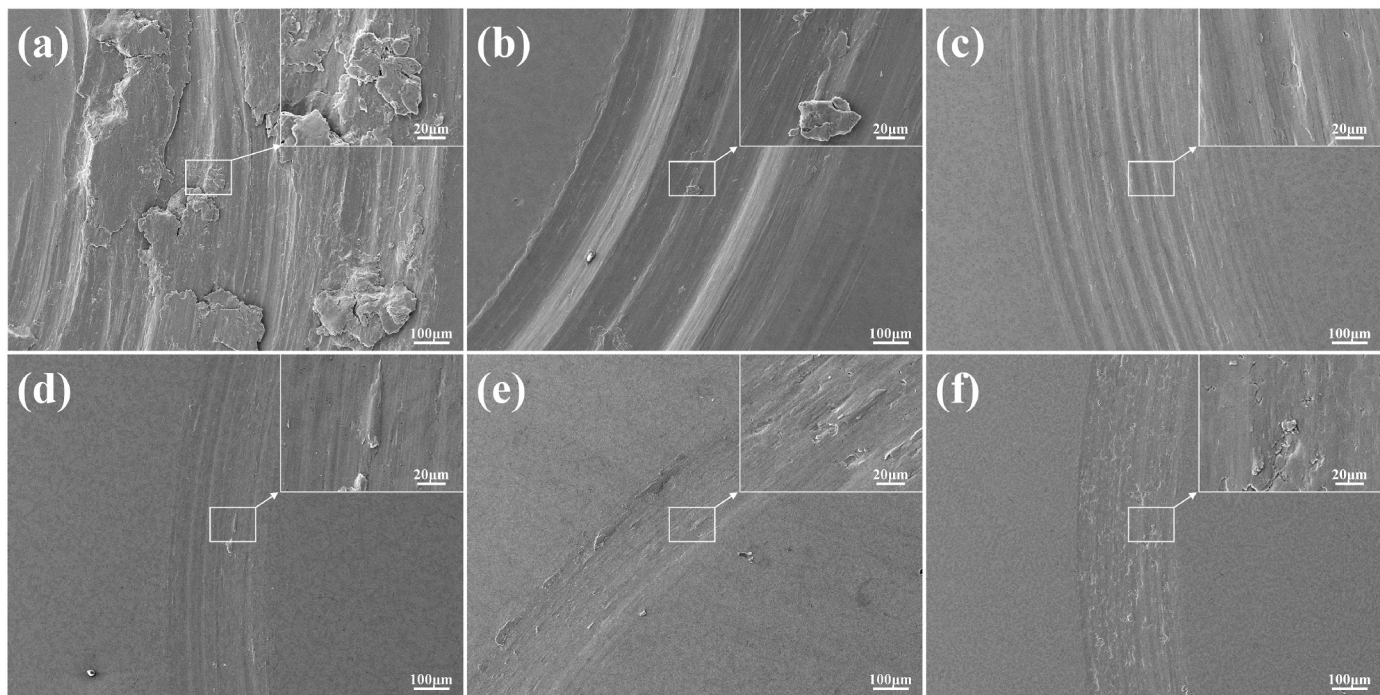


Fig. 14. SEM images of worn surfaces of FeCrNiCuTi_x alloys ($x = 0, 0.2, 0.4, 0.6, 0.8$, and 1).

Acknowledgments

This work was supported by China Postdoctoral Science Foundation (Grant No. 2022M711989), the National Natural Science Foundation of China (Grant No. 52004264), Sichuan Science and Technology Program (Grant No. 2022YFSY0019), Double Thousand Plan of Jiangxi Province (jxsq2020105012), and Program of Ganzhou Suquzhiguang (GZSQZG202101009).

References

- [1] Yeh JW, Chen SK, Lin SJ, Gan JY, Chin TS, Shun TT, Tsau CH, Chang SY. Nanostructured high-entropy alloys with multiple principal elements: novel alloy design concepts and outcomes. *Adv Eng Mater* 2004;6:299–303. <https://doi.org/10.1002/adem.200300567>.
- [2] Cantor B, Chang ITH, Knight P, Vincent AJB. Microstructural development in equiatomic multicomponent alloys. *Mater Sci Eng* 2004;375–377:213–8. <https://doi.org/10.1016/j.msea.2003.10.257>.
- [3] Yeh JW, Chang SY, Hong YD, Chan SK, Lin SJ. Anomalous decrease in X-ray diffraction intensities of Cu–Ni–Al–Co–Cr–Fe–Si alloy systems with multi-principal elements. *Mater Chem Phys* 2007;103:41–6. <https://doi.org/10.1016/j.matchemphys.2007.01.003>.
- [4] Zhang Y, Zuo TT, Tang Z, Gao MC, Dahmen KA, Liaw PK, Lu ZP. Microstructures and properties of high-entropy alloys. *Prog Mater Sci* 2014;61:1–93. <https://doi.org/10.1016/j.pmatsci.2013.10.001>.
- [5] Tsai KY, Tsai MH, Yeh JW. Sluggish diffusion in Co–Cr–Fe–Mn–Ni high-entropy alloys. *Acta Mater* 2013;61:4887–97. <https://doi.org/10.1016/j.actamat.2013.04.058>.
- [6] Ranganathan S. Alloyed pleasures: multimetallic cocktails. *Curr Sci* 2003;85:10. <https://doi.org/10.1038/nature02146>.
- [7] Cai YP, Wang GJ, Ma YJ, Cao ZH, Meng XK. High hardness dual-phase high entropy alloy thin films produced by interface alloying. *Scripta Mater* 2019;162:281–5. <https://doi.org/10.1016/j.scriptamat.2018.11.004>.
- [8] Yi JJ, Wang L, Zeng L, Xu MQ, Yang L, Tang S. Excellent strength-ductility synergy in a novel single-phase equiatomic CoFeNiTiV high entropy alloy. *Int J Refract Metals Hard Mater* 2021;95:1. <https://doi.org/10.1016/j.ijrmhm.2020.105416>.
- [9] Chuang MH, Tsai MH, Wang WR, Lin SJ, Yeh JW. Microstructure and wear behavior of $\text{Al}_x\text{Co}_{1-x}\text{CrFeNi}_{1-x}\text{Ti}_y$ high-entropy alloys. *Acta Mater* 2011;59:6308–17. <https://doi.org/10.1016/j.actamat.2011.06.041>.
- [10] Cheng HG, Pan ZM, Fu Y, Wang XF, Wei Y, Luo H, Li XG. Review—corrosion-resistant high-entropy alloy coatings: a review. *J Electrochem Soc* 2021;168:11. <https://doi.org/10.1149/1945-7111/ac34d0>.
- [11] Senkov ON, Wilks GB, Scott JM, Miracle DB. Mechanical properties of $\text{Nb}_{25}\text{Mo}_{25}\text{Ta}_{25}\text{W}_{25}$ and $\text{V}_{20}\text{Nb}_{20}\text{Mo}_{20}\text{Ta}_{20}\text{W}_{20}$ refractory high entropy alloys. *Intermetallics* 2011;19:698–706. <https://doi.org/10.1016/j.intermet.2011.01.004>.
- [12] Liu CM, Wang HM, Zhang SQ, Tang HB, Zhang AL. Microstructur-e and oxidation behavior of new refractory high entropy alloys. *J Alloys Compd* 2014;583:162–9. <https://doi.org/10.1016/j.jallcom.2013.08.102>.
- [13] Tan MT, Meng L, Fang S, Lin C, Ke LS, Yu ZH, Qu JK, Qi T. Organizational evolution during performance meritocracy of $\text{AlSi}_{0.5}\text{Cr}_x\text{Co}_{0.2}\text{Ni}$ lightweight high entropy alloys. *Crystals* 2022;12:12. <https://doi.org/10.3390/crys12121828>.
- [14] Ren C, Sun K, Jia YF, Zhang NZ, Jia YD, Wang G. Effect of Mo addition on the microstructural evolution and mechanical properties of Fe–Ni–Cr–Mn–Al–Ti high entropy alloys. *Mater Sci Eng, A* 2023;864:1444579. <https://doi.org/10.1016/j.msea.2023.144579>.
- [15] Xie TJ, Jin FS, Qin Lei, Long SL, Yi YL, Zhou SF. Effects of La and Y on the microstructure and mechanical properties of $\text{NbMoTiVS}_{0.3}$ refractory high entropy alloys. *J Alloys Compd* 2023;931:167464. [https://doi.org/10.1016/S1003-6326\(21\)65513-9](https://doi.org/10.1016/S1003-6326(21)65513-9).
- [16] Stepanov ND, Yurchenko NYu, Skibin DV, Tikhonovsky MA, Salishchev GA. Structure and mechanical properties of the $\text{AlCr}_x\text{NbTiV}$ ($x = 0, 0.5, 1, 1.5$) high entropy alloys. *J Alloys Compd* 2015;652:266–80. <https://doi.org/10.1016/j.jallcom.2015.08.224>.
- [17] Tan MT, Meng L, Lin C, Ke LS, Liu YD, Qu Jingkui, Qi T. Variation of microstructures and properties of $\text{Co}_{0.2}\text{CrAlNi}$ high entropy alloy doped Si. *J Alloys Compd* 2022;927:167081. <https://doi.org/10.1016/j.jallcom.2022.167081>.
- [18] Stepanov ND, Shaysultanov DG, Salishchev GA, Tikhonovsky MA, Oleynik EE, Tortika AS, Senkov ON. Effect of V content on microstructure and mechanical properties of the CoCrFeMnNiV_x high entropy alloys. *J Alloys Compd* 2015;628:170–85. <https://doi.org/10.1016/j.jallcom.2014.12.157>.
- [19] Wu MY, Chen K, Xu Z, Li DY. Effect of Ti addition on the sliding wear behavior of AlCrFeCoNi high-entropy alloy. *Wear* 2020;462–3. <https://doi.org/10.1016/j.wear.2020.203493>.
- [20] Chan SN, Hsueh CH. Effects of La addition on the microstructure and mechanical properties of CoCrNi medium entropy alloy. *J Alloys Compd* 2022;894:162401. <https://doi.org/10.1016/j.jallcom.2021.162401>.
- [21] Hong X, Hsueh CH. Effects of yttrium addition on microstructures and mechanical properties of CoCrNi medium entropy alloy. *Intermetallics* 2022;140:107405. <https://doi.org/10.1016/j.intermet.2021.107405>.
- [22] Wang G, Li TL, Liao YC, Li CL, Jang JSC, Hsueh CH. Hardness and strength enhancements of CoCrFeMnNi high-entropy alloy with Nd doping. *Mater Sci Eng, A* 2019;764:138192. <https://doi.org/10.1016/j.msea.2019.138192>.
- [23] Lin YS, Lu YC, Hsueh CH. Strengthening of CoCrNi medium entropy alloy with gadolinium additions. *Vacuum* 2023;211:111969. <https://doi.org/10.1016/j.vacuum.2023.111969>.
- [24] Chen Z, Chen WP, Wu BY, Cao XY, Liu LS, Fu ZQ. Effects of Co and Ti on microstructure and mechanical behavior of $\text{Al}_{0.75}\text{FeNiCrCo}$ high entropy alloy prepared by mechanical alloying and spark plasma sintering. *Mater Sci Eng* 2015;648:217–24. <https://doi.org/10.1016/j.msea.2015.08.056>.
- [25] Wang XF, Zhang Y, Qiao Y, Chen GL. Novel microstructure and properties of multicomponent CoCrCuFeNiTi_x alloys. *Intermetallics* 2007;15:357–62. <https://doi.org/10.1016/j.intermet.2006.08.005>.

- [26] Shun TT, Chang LY, Shiu MH. Microstructures and mechanical properties of multiprincipal component CoCrFeNiTi_x alloys. *Mater Sci Eng, A* 2012;526:170–4. <https://doi.org/10.1016/j.msea.2012.06.075>.
- [27] Lin C, Meng L, Tan MT, Ke LS, Qi T. Microstructures and properties of Cr_x-FeNiCu_{0.5}Ti_{0.5} high-entropy alloys for corrosion resistance. *Intermetallics* 2023; 153:107781. <https://doi.org/10.1016/j.intermet.2022.107781>.
- [28] Chae MJ, Sharma A, Oh MC, Ahn B. Lightweight AlCuFeMnMgTi high entropy alloy with high strength-to-density ratio processed by powder metallurgy, metals and materials. *International* 2020;27:629–38. <https://doi.org/10.1007/s12540-020-00823-5>.
- [29] Oh MC, Sharma A, Lee H, Ahn B. Phase separation and mechanical b-behavior of AlCoCrFeNi-X (X = Cu, Mn, Ti) high entropy alloys processed via powder metallurgy. *Intermetallics* 2021;139:107369. <https://doi.org/10.1007/s12540-020-00823-5>.
- [30] Ye XC, Wang T, Xu ZY, Liu C, Wu HH, Zhao GW, Fang D. Effect of Ti content on microstructure and mechanical properties of CuCoFeNi high-entropy alloys. *Int J Miner Metall Mater* 2020;27:1326–31. <https://doi.org/10.1007/s12613-020-2024-1>.
- [31] Macdonald BE, Fu Z, Zheng B, Chen W, Lin Y, Chen F, Zhang L, Ivanisenko J, Zhou Y, Hahn H, Lavernia EJ. Recent progress in high E-ntropy alloy research. *JOM* 2017;69:2024–31. <https://doi.org/10.1007/s11837-017-2484-6>.
- [32] Chae MJ, Lee H, Sharma A, Ahn B. Effect of light (X = Mg, Si) and heavy (X = Zn) metals on the microstructural evolution and densification of AlCuFeMnTi-X high-entropy alloy processed by advanced powder metallur-gy. *Powder Metall* 2021;64: 228–34. <https://doi.org/10.1080/00325899.2021.1909212>.
- [33] Takeuchi A, Inoue A. Classification of bulk metallic glasses by atomic size difference, heat of mixing and period of constituent elements and its application to characterization of the main alloying element. *Mater Trans* 2005;46:2817–29. <https://doi.org/10.2320/matertrans.46.2817>.
- [34] Huang L, Wang XJ, Huang BX, Zhao XC, Chen H, Wang CZ. Effect of Cu segregation on the phase transformation and properties of AlCrFeNiTiCu_x high-entropy alloys. *Intermetallics* 2022;140:107397. <https://doi.org/10.1016/j.intermet.2021.107397>.
- [35] Cheng BQ, Ceriotti M, Tribello GA. Classical nucleation theory predicts the shape of the nucleus in homogeneous solidification. *J Chem Phys* 2020;152:044103. <https://doi.org/10.1063/1.5134461>.
- [36] Li ZY, Fu LM, Peng J, Zheng H, Shan AD. Effect of annealing on microstructure and mechanical properties of an ultrafine-structured Al-containing FeCoCrNiMn high-entropy alloy produced by severe cold rolling. *Mater Sci Eng* 2020;786:139446. <https://doi.org/10.1016/j.msea.2020.139446>.
- [37] Sharma A, Lee H, Ahn B. Effect of additive elements (x = Cr, Mn, Zn, Sn) on the phase evolution and thermodynamic complexity of AlCuSiFe-x high entropy alloys fabricated via. *Powder Metallurgy, Metals and Materials International* 2022;28: 2216–24. <https://doi.org/10.1007/s12540-021-01125-0>.
- [38] Li WD, Xie D, Li DY, Zhang Y, Gao YF, Liaw PK. Mechanical behavior of high-entropy alloys. *Prog Mater Sci* 2021;118:100777. <https://doi.org/10.1016/j.pmatsci.2021.100777>.
- [39] Chen T, Tan L, Lu Z, Xu H. The effect of grain orientation on nanoindentation behavior of model austenitic alloy Fe-20Cr-25Ni. *Acta Mater* 2017;138:83–91. <https://doi.org/10.1016/j.actamat.2017.07.028>.
- [40] Li JX, Yamanaka K, Chiba A. Calculation-driven design of offequiatomic high-entropy alloys with enhanced solid-solution strengthening. *Mater Sci Eng* 2021; 817:141359. <https://doi.org/10.1016/j.msea.2021.141359>.
- [41] Zhang LJ, Zhangha MD, Zhou Z, Fana JT, Cui P, Yu PF, Jing Q, Ma MZ, Liaw PK, Li G, Liua RP. Effects of rare-earth element, Y, additions on the microstructure and mechanical properties of CoCrFeNi high entropy alloy. *Mater Sci Eng, A* 2018;725: 437–46. <https://doi.org/10.1016/j.msea.2018.04.058>.
- [42] Miracle DB, Senkov ON. A critical review of high entropy alloys and related concepts. *Acta Mater* 2017;122:448–511. <https://doi.org/10.1016/j.actamat.2016.08.081>.
- [43] Zhang ZJ, Zhang BS, Zhu SS, Yu YQ, Wang ZZ, Zhang XC, L-u B. Microstructural characteristics and enhanced wear resistance of nanoscale Al₂O₃/13 wt%TiO₂-reinforced CoCrFeMnNi high entropy coatings. *Surf Coating Technol* 2021;412: 127019. <https://doi.org/10.1016/j.surcoat.2021.127019>.
- [44] Moazzzen P, Toroghinejad MR, Cavaliere P. Effect of Iron content on the microstructure evolution, mechanical properties and wear resistance of Fe_xCoCrNi high-entropy alloy system produced via MA-SPS. *J Alloys Compd* 2021;870: 159410. <https://doi.org/10.1016/j.jallcom.2021.159410>.